Estimation of geometric properties of three-component signals for system monitoring

Pierre Granjon, Gailene Shih-Lyn Phua

Estimation of geometric properties of three-component signals for system monitoring

Pierre Granjon[a,b,*], Gailene Shih Lyn Phua[a,b]

[a] *Univ. Grenoble Alpes, GIPSA-Lab, F-38000 Grenoble, France*
[b] *CNRS, GIPSA-Lab, F-38000 Grenoble, France*

Abstract

Most methods for condition monitoring are based on the analysis and characterization of physical quantities that are three-dimensional in nature. Plotted in a three-dimensional Euclidian space as a function of time, such quantities follow a trajectory whose geometric characteristics are representative of the state of the monitored system. Usual condition monitoring techniques often study the measured quantities component by component, without taking into account their three-dimensional nature and the geometric properties of their trajectory. A significant part of the information is thus ignored. This article details a method dedicated to the analysis and processing of three-component quantities, capable of highlighting the special geometric features of such data and providing complementary information for condition monitoring. The proposed method is applied to two experimental cases: bearing fault monitoring in rotating machines, and voltage dips monitoring in three-phase power networks. In this two cases, the obtained results are promising and show that the estimated geometric indicators lead to complementary information that can be useful for condition monitoring.

Keywords: three-component signals, geometric properties, Frenet-Serret frame, bearing faults, voltage dips, condition monitoring

1. Introduction

Safety and economical constraints force industries to continuously improve their maintenance strategies. When possible, predictive or condition-based maintenance is used as it helps reducing repair time and cost, improve safety, and avoid economic losses. Very often, condition monitoring techniques rely on the characterization of inherently three-component physical quantities, which are frequently encountered in technological processes. A first example is the monitoring of three-phase electrical systems, based on three-phase electrical

*Corresponding author
Email addresses: pierre.granjon@gipsa-lab.grenoble-inp.fr (Pierre Granjon), gailene.phua@gipsa-lab.grenoble-inp.fr (Gailene Shih Lyn Phua)

measurements like voltages and currents. Another common example is the monitoring of mechanical systems, based on three-axis vibration or three-dimensional displacement measurements. In order to obtain efficient fault indicators, such three-component signals are usually analyzed with the usual marginal and/or joint analysis tools in the time domain (correlation functions and/or correlation matrices) as well as in the frequency domain (spectra and/or spectral matrices) [1]. However, three-component signals also contain another type of information which is completely different in nature: their geometric properties. When a three-component signal is represented in three-dimensional Euclidean space, it follows a particular trajectory. The geometric properties of this trajectory may contain information concerning the state of the monitored system from which the signal was acquired. This approach has already been successfully proposed in the field of system monitoring with two-component signals [2] by using complex-valued signal processing tools [3]. It is for example the case for orbit shape analysis used to detect faults in rotating machines [4, 5, 6], and for voltage dips detection and classification in power networks [7]. However, and as previously mentioned, usual condition monitoring methods do not take into account the three-dimensional geometric characteristics of the trajectory of the measured three-component quantities. As a consequence, a significant part of the diagnostic information is ignored.

This research work aims to fill this gap by developing a method to estimate the geometric properties of three-component signals which takes into account all three components at the same time. The proposed method relies on basic concepts of differential geometry of space curves such as the Frenet-Serret frame and formulas, curvature and torsion, and leads to local geometric descriptors of the three-dimensional curves followed by three-component signals. The method takes as its input a three-component signal, i.e. a time series where three data points are available at each time t. These data are then considered as Cartesian coordinates defining the position of the measured signal at time t in a three-dimensional Euclidean space. However, raw signals measured in real-life systems tend to be complicated and thus lead to trajectories with complicated geometric properties. To simplify matters, as in spectral analysis, the signal is simplified by analyzing only one frequency component. This sinusoidal signal, composed of three sinusoids of the same frequency, follows a trajectory in three-dimensional space which is elliptical in shape, and the geometric properties of the corresponding trajectory can be analyzed more easily. This is what the proposed method is for: to estimate the geometric properties of the trajectory of a three-component sinusoidal signal in three-dimensional space. The estimated geometric properties can then be used to elaborate stand-alone or complementary fault indicators for condition monitoring purposes.

In order to validate this approach, the proposed method is applied to two different experimental cases: voltage dips monitoring in three-phase power networks, and bearing faults monitoring in rotating machines. In this two cases, the results obtained are promising and show that the estimated geometric indicators lead to complementary information that can be useful for condition monitoring purpose.

The previous ideas are detailed in this article, which is organized as follows. The theoretical foundations of the proposed method are presented in section 2, which includes the basic differential geometry tools used, the definition of the three-component signal of interest, as well as the geometric properties to be estimated. The structure of the algorithm developed

to estimate these geometric properties is then described in section 3, along with the details of its estimation performance with respect to various parameters. The experimental results obtained by this algorithm in the context of the two application examples of voltage dips monitoring in three-phase power networks and bearing faults monitoring in rotating machines are given in sections 4 and 5 respectively. Finally, the article ends with concluding remarks including a summary and suggestions of possible future work.

2. Geometric properties of three-component sinusoidal signals

2.1. Differential geometry of space curves

A natural way of defining a curve is through differentiable functions. Let I be an open interval in the real line $\mathbb{R}$ and $\mathbf{r}$ be a function from I to $\mathbb{R}^3$ as defined in Eq. (1) where $\mathbb{R}^3$ denotes the set of triples of real numbers and r_1, r_2 and r_3 are differentiable functions of t.

$$\begin{aligned} \mathbf{r}\colon I &\to \mathbb{R}^3 \\ t &\mapsto (r_1(t), r_2(t), r_3(t)) \end{aligned} \tag{1}$$

$\mathbf{r}$ is called a parametrized differentiable curve and the variable t is the parameter of the curve [8, 9]. A curve $\mathbf{r}$ maps each t in I into a point $\mathbf{r}(t) = (r_1(t), r_2(t), r_3(t))$ in $\mathbb{R}^3$ in such a way that the functions r_1, r_2 and r_3 are differentiable. In other words, at each t in some open interval I, $\mathbf{r}$ is located at the point $\mathbf{r}(t) = (r_1(t), r_2(t), r_3(t))$ in $\mathbb{R}^3$, and the corresponding curve can be pictured as a trip taken by a moving point $\mathbf{r}$ in $\mathbb{R}^3$.

The Frenet-Serret frame is the most natural choice to study the local geometric properties of a curve. It can be interpreted as a moving reference frame that provides a local coordinate system at each point of the curve, facilitating the definition of geometric properties of the curve in the neighborhood of each point [10]. The Frenet-Serret frame is composed of three orthogonal unit vectors $\mathbf{T}(t)$, $\mathbf{N}(t)$, and $\mathbf{B}(t)$, respectively called the tangent, normal and binormal vector. Their definition is given by the three following equations [9, 11]:

$$\mathbf{T}(t) = \frac{\mathbf{r}'(t)}{\|\mathbf{r}'(t)\|} \tag{2}$$

$$\mathbf{N}(t) = \frac{\mathbf{T}'(t)}{\|\mathbf{T}'(t)\|} = \frac{\mathbf{r}'(t) \times (\mathbf{r}''(t) \times \mathbf{r}'(t))}{\|\mathbf{r}'(t)\| \, \|\mathbf{r}''(t) \times \mathbf{r}'(t)\|} \tag{3}$$

$$\mathbf{B}(t) = \mathbf{T}(t) \times \mathbf{N}(t) = \frac{\mathbf{r}'(t) \times \mathbf{r}''(t)}{\|\mathbf{r}'(t) \times \mathbf{r}''(t)\|} \tag{4}$$

where $\mathbf{r}'(t) = \frac{\mathrm{d}\mathbf{r}(t)}{\mathrm{d}t}$ is the derivative of $\mathbf{r}(t)$, $\times$ denotes the cross-product between two vectors and $\|\mathbf{r}(t)\|$ is the norm of $\mathbf{r}(t)$ defined by:

$$\|\mathbf{r}(t)\| = \sqrt{r_1(t)^2 + r_2(t)^2 + r_3(t)^2} \tag{5}$$

As shown in Fig. 1, these three vectors form an orthonormal basis spanning $\mathbb{R}^3$, and each of them contains a precise geometric information about the curve. The tangent vector $\mathbf{T}(t)$

points in the direction of motion of $\mathbf{r}$ at any point t. $\mathbf{N}(t)$ is normal to the direction of motion of $\mathbf{r}$ and indicates the direction in which $\mathbf{r}$ is turning at t. As shown in Eq. (4), the binormal vector $\mathbf{B}(t)$ is defined as the cross product between $\mathbf{T}(t)$ and $\mathbf{N}(t)$, and is thus orthogonal to both of them. This vector defines the osculating plane spanned by the tangent and normal vectors in which the curve $\mathbf{r}$ lies at t such as to have a second order contact with this plane [9].

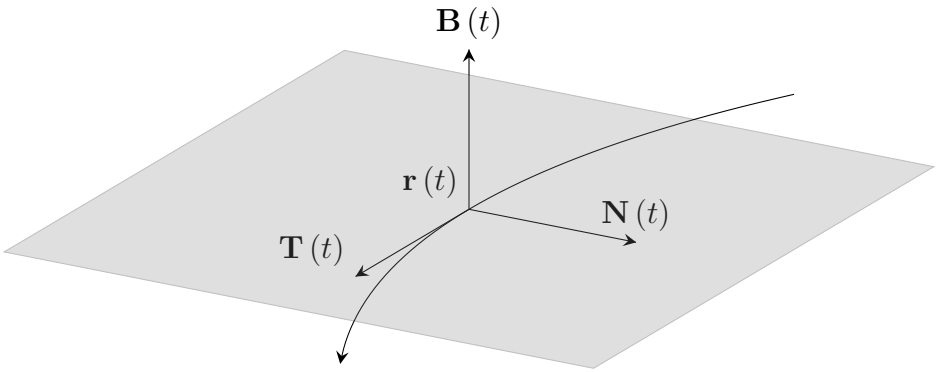

Figure 1: Tangent $\mathbf{T}(t)$, normal $\mathbf{N}(t)$ and binormal $\mathbf{B}(t)$ vectors of the Frenet-Serret frame and the osculating plane (in gray) at t of a space curve $\mathbf{r}(t)$.

The Frenet-Serret formulas express the derivatives $\mathbf{T}'(t)$, $\mathbf{N}'(t)$ and $\mathbf{B}'(t)$ in terms of $\mathbf{T}(t)$, $\mathbf{N}(t)$ and $\mathbf{B}(t)$. They can be interpreted as a set of first order differential equations verified by the Frenet-Serret frame for a given parametrized differentiable curve $\mathbf{r}$, and are given in matrix notation in the following equation:

$$\begin{bmatrix} \mathbf{T}'(t) \\ \mathbf{N}'(t) \\ \mathbf{B}'(t) \end{bmatrix} = \|\mathbf{r}'(t)\| \begin{bmatrix} 0 & \kappa(t) & 0 \\ -\kappa(t) & 0 & \tau(t) \\ 0 & -\tau(t) & 0 \end{bmatrix} \begin{bmatrix} \mathbf{T}(t) \\ \mathbf{N}(t) \\ \mathbf{B}(t) \end{bmatrix} \tag{6}$$

where the scalars $\kappa(t)$ and $\tau(t)$ are the curvature and the torsion of the curve at point $\mathbf{r}(t)$, respectively. Using that $\mathbf{N}(t)$ is a unit vector, the first line of Eq. (6) leads to $\|\mathbf{T}'(t)\| = \|\mathbf{r}'(t)\| \, |\kappa(t)|$. The curvature $\kappa(t)$ is therefore related to the rate of change of the tangent vector, and represents the tendency of $\mathbf{r}(t)$ to deviate from the local direction of motion. This positive scalar measures how sharp $\mathbf{r}$ is curving at each point: the sharper the bend, the larger the curvature. For example, the curvature of a circular curve is constant at every point and equal to the inverse of the circle radius, while the curvature of a straight line is null at every point. Similarly, the third line of Eq. (6) leads to $\|\mathbf{B}'(t)\| = \|\mathbf{r}'(t)\| \, |\tau(t)|$. Hence, the torsion $\tau(t)$ is directly related to the rate of change of the binormal vector $\mathbf{B}(t)$, and measures at each point the tendency of $\mathbf{r}(t)$ to deviate from the osculating plane. For example, if $\mathbf{r}$ is a plane curve, the torsion $\tau(t)$ is null whatever t. In that case the binormal vector is constant since $\mathbf{B}'(t) = 0$, and the curve $\mathbf{r}(t)$ lies in the plane orthogonal to $\mathbf{B}$, that is the osculating plane. Finally, as for the three unit vectors defining the Frenet-Serret frame,

the curvature and torsion can be expressed in terms of $\mathbf{r}(t)$ and its first derivatives [9, 11]:

$$\kappa(t) = \frac{\|\mathbf{r}'(t) \times \mathbf{r}''(t)\|}{\|\mathbf{r}'(t)\|^3} \tag{7}$$

$$\tau(t) = \frac{(\mathbf{r}'(t) \times \mathbf{r}''(t)) \cdot \mathbf{r}'''(t)}{\|\mathbf{r}'(t) \times \mathbf{r}''(t)\|^2} \tag{8}$$

where $\cdot$ is the dot product between two vectors.

2.2. Interesting geometric indicators

Several quantities presented in this section can be used to locally characterize the geometry of the curve followed by a three-component signal. The curvature $\kappa(t)$ and the torsion $\tau(t)$ defined in Eq. (7) and (8) are clearly interesting geometric indicators, and give simple and precise information on the shape of the curve. This is confirmed by the fundamental theorem of space curves [8, 11], stating that for a given curvature κ and torsion τ, there exists exactly one space curve $\mathbf{r}$ such that κ is the curvature and τ is the torsion of $\mathbf{r}$, this curve being determined except for its orientation and position in space.

Another interesting geometric indicator is the osculating plane or equivalently the binormal vector $\mathbf{B}(t)$ defined in Eq. (4). Indeed, this vector indicates in which plane the curve lies at t, and gives the orientation of the curve in space contrary to the two previous indicators.

The last interesting indicator is the norm of $\mathbf{r}(t)$ defined in Eq. (5). This quantity measures the distance between the point $\mathbf{r}(t)$ and the origin of the static Euclidian frame. Consequently, it can be interpreted as an instantaneous amplitude of the three-component signal, or similarly as the global amount of signal at time t.

2.3. The case of three-component sinusoidal signals

As previously mentioned, this research work focuses on condition monitoring applications where the measured three-component signals can be considered as quasi-periodic, i.e. as a sum of sine waves. Consequently, it makes sense to study in detail the geometric characteristics of simple three-component sinusoidal signals by using the different tools presented in the previous paragraph.

A signal is a three-component sinusoidal signal if each of its components is a sine wave with the same frequency. A three-component sinusoidal signal $\mathbf{r}$ can therefore be written mathematically as in Eq. (9), where A_i and φ_i for $i \in \{1, 2, 3\}$ denote the amplitude and phase of the sinusoids and f_0 is their frequency.

$$\mathbf{r}(t) = \begin{bmatrix} r_1(t) \\ r_2(t) \\ r_3(t) \end{bmatrix} = \begin{bmatrix} A_1 \sin(2\pi f_0 t + \varphi_1) \\ A_2 \sin(2\pi f_0 t + \varphi_2) \\ A_3 \sin(2\pi f_0 t + \varphi_3) \end{bmatrix} \tag{9}$$

This equation clearly shows that such a signal can be considered as a parametrized differentiable 3D space curve where t is the parameter on which the differential geometric approach presented in the last paragraph can be directly applied.

In this context, it has been demonstrated in [12] that under very general conditions, a three-component sinusoidal signal with constant amplitudes, phases and frequency follows an elliptical trajectory in a three-dimensional Euclidean frame. This elliptical trajectory can be seen as a Lissajous figure in 3D, and is sometimes referred to as a 3D polarization ellipse [13]. Using the general expression of three-component sinusoidal signals given in Eq. (9) and the definition of the desired geometric indicators given in Eq. (5), (7), (8), the theoretical expression of the signal norm, curvature and torsion are obtained:

$$\|\mathbf{r}(t)\| = \sqrt{A_1^2 \sin^2(2\pi f_0 t + \varphi_1) + A_2^2 \sin^2(2\pi f_0 t + \varphi_2) + A_3^2 \sin^2(2\pi f_0 t + \varphi_3)} \tag{10}$$

$$\kappa(t) = \frac{\sqrt{(A_2A_3)^2 \sin^2(\varphi_2 - \varphi_3) + (A_1A_3)^2 \sin^2(\varphi_3 - \varphi_1) + (A_1A_2)^2 \sin^2(\varphi_1 - \varphi_2)}}{\sqrt{\left(A_1^2 \cos^2(2\pi f_0 t + \varphi_1) + A_2^2 \cos^2(2\pi f_0 t + \varphi_2) + A_3^2 \cos^2(2\pi f_0 t + \varphi_3)\right)^3}} \tag{11}$$

$$\tau(t) = 0 \tag{12}$$

One interesting result is that the torsion is null for such signals, meaning that the corresponding trajectories are as expected plane curves, with a plane orthogonal to the binormal vector obtained with Eq. (4):

$$\mathbf{B}(t) = \frac{1}{\delta} \begin{bmatrix} A_2A_3 \sin(\varphi_2 - \varphi_3) \\ A_3A_1 \sin(\varphi_3 - \varphi_1) \\ A_1A_2 \sin(\varphi_1 - \varphi_2) \end{bmatrix} \tag{13}$$

where $\delta = \sqrt{(A_2A_3)^2 \sin^2(\varphi_2 - \varphi_3) + (A_3A_1)^2 \sin^2(\varphi_3 - \varphi_1) + (A_1A_2)^2 \sin^2(\varphi_1 - \varphi_2)}$.
Eq. (10) to (13) give the theoretical values of the main geometric properties of the space curve corresponding to a three-component sinusoidal signal, and Figure 2 shows an example of application of these relations for a particular signal. From Fig. 2b and 2c, it can be seen that the norm and the curvature of $\mathbf{r}$ do vary with time t for an ellipse, while the torsion is null in Fig. 2d and the binormal vector is constant in Fig. 2e as expected. By comparing Fig. 2f and Fig. 2g giving the 3D representation of $\mathbf{r}$ and $\mathbf{B}$, it can finally be verified that the binormal vector points in the direction perpendicular to the osculating plane that the ellipse is in.

The next section presents a simple algorithm dedicated to the estimation of the geometric properties of interest for three-component signals, and a brief description of its estimation performance in the case of noisy measurements.

3. Estimation algorithm

3.1. General structure

In the last section, the norm $\|\mathbf{r}(t)\|$, curvature $\kappa(t)$, torsion $\tau(t)$ and binormal vector $\mathbf{B}(t)$ have been chosen to characterize the geometry of the trajectory followed by a three-component sinusoidal signal. Eq. (5), (7), (8) and (4) show that these geometric properties

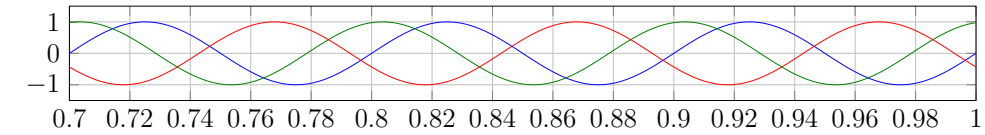

(a) the three sinusoidal components of $\mathbf{r}(t)$

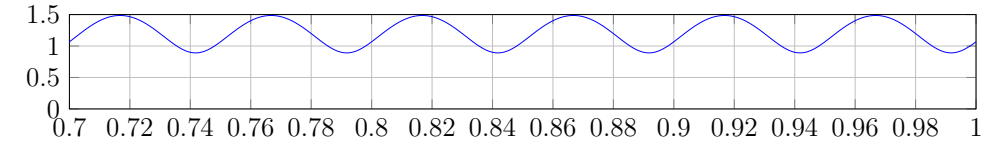

(b) $\|\mathbf{r}(t)\|$

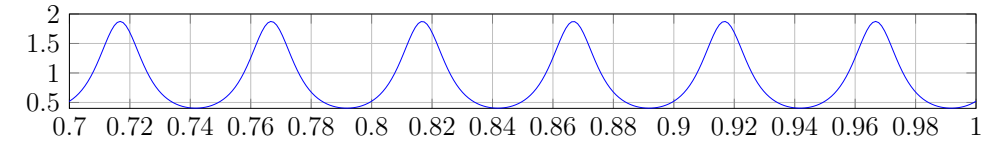

(c) $\kappa(t)$

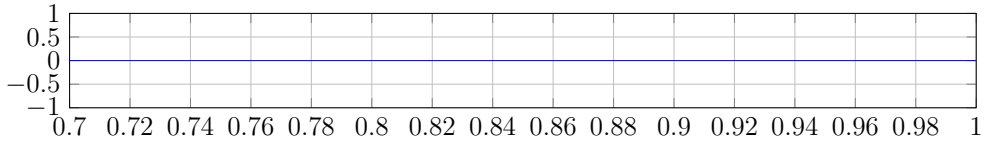

(d) $\tau(t)$

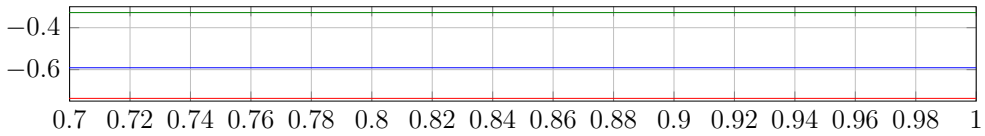

(e) $\mathbf{B}(t)$ in Cartesian coordinates

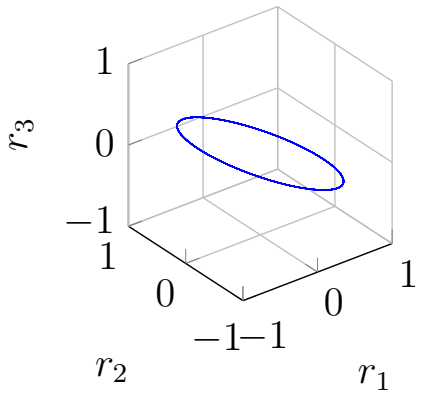

(f) $\mathbf{r}(t)$ in the 3D Euclidian space

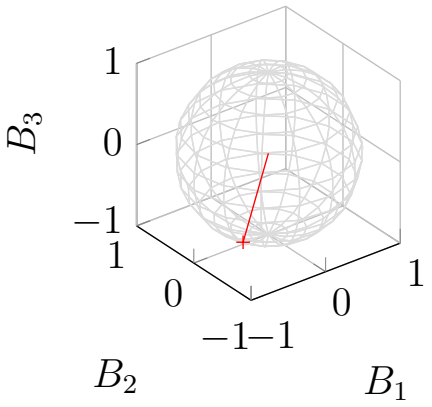

(g) $\mathbf{B}(t)$ in the unit sphere

Figure 2: A three-component sinusoidal signal $\mathbf{r}(t)$ with $f_0 = 10$ Hz, $A_1 = A_2 = A_3 = 1$, $[\varphi_1, \varphi_2, \varphi_3] = \left[0, \frac{3\pi}{7}, \frac{8\pi}{7}\right]$, and the theoretical values of its main geometric properties.

can be calculated in terms of the values of the position vector $\mathbf{r}(t)$ and its first three derivatives with respect to time t, $\mathbf{r}'(t)$, $\mathbf{r}''(t)$ and $\mathbf{r}'''(t)$. This remark leads to the three-step algorithm illustrated in Fig. 3, already proposed and detailed in [14] and [12] to estimate the four previous geometric properties of a three-component signal $\mathbf{x}$ at a given frequency.

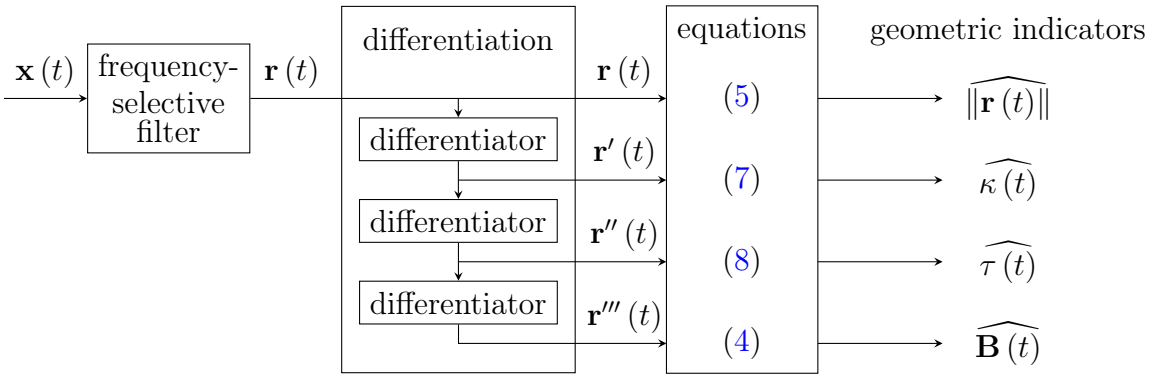

Figure 3: Block diagram of the proposed estimation algorithm.

Measured signals usually contain more than one frequency component including noise, and it is therefore essential to filter such signals first to remove noise and all unwanted frequency components leaving only one frequency component. To carry out this step, a classical linear phase finite impulse response (FIR) frequency-selective filter [15], which can be a lowpass, bandpass or highpass filter depending on the value of the selected frequency f_0, is used. This first step produces the three-component sinusoidal signal $\mathbf{r}$ following an elliptical trajectory from which the geometric properties can be further estimated and analyzed. As can be seen from the mathematical definitions of the four geometric properties of interest, the next necessary step is the differentiation of $\mathbf{r}$, realized thanks to a simple linear phase FIR differentiator filter. Instead of a full-band differentiator, a partial-band differentiator adapted to the selected frequency f_0 is used in order to avoid amplifying possible residual high frequency components and maximize the signal-to-noise ratio (SNR) at the output of each differentiator [16]. Since $\mathbf{r}$ needs to be differentiated three times, the same differentiator filter is applied three times consecutively to $\mathbf{r}$. The use of the frequency-selective and differentiator FIR filters means that there are signal delays that need to be managed after each application of a filter to synchronize the signals. Now that the position vector $\mathbf{r}$ and its first three derivatives are estimated, the four geometric properties of interest, $\|\mathbf{r}\|$, κ, τ and $\mathbf{B}$, can be computed. The third and final step of the estimation algorithm illustrated in the block diagram of Fig. 3 is to compute these desired geometric properties using the four equations (5), (7), (8) and (4), where only basic mathematical operators (division, square root, dot product, cross product) are needed. Once the geometric properties are computed, their time evolution can be further plotted and analyzed, which is done in the following section using a synthetic signal.

3.2. Application to a synthetic signal

The proposed algorithm is applied to a synthetic signal including a change in amplitude and phase with the purpose of illustrating its estimating and tracking capabilities. A three-component sinusoidal signal of frequency $f_0 = 10$ Hz is first generated with a continuous change in its amplitude (from $[20, 20, 20]$ to $[25, 25, 25]$) and phase (from $\left[0, \frac{3\pi}{7}, \frac{8\pi}{7}\right]$ to $\left[0, \frac{3\pi}{7}, \frac{5\pi}{7}\right]$) between 10 s and 10.0625 s. A centered and stationary white Gaussian noise with variance 126 is then added to each sine wave to obtain a noisy three-component sinusoidal signal $\mathbf{x}$, with a global signal-to-noise ratio on each component close to 2 dB before the change and to 4 dB after the change. The sampling frequency is set to $f_s = 1024$ Hz.

The specifications of the two filters used in the proposed algorithm are set according to the frequency of the sinusoidal components to be characterized. The frequency-selective filter is a bandpass filter with a central frequency equal to the chosen frequency $f_0 = 10$ Hz, a bandwidth of 2 Hz and a transition band of 1 Hz, while the bandwidth of the partial-band differentiator filter ends at 11 Hz and its stopband starts at 12 Hz. Figure 4 shows the magnitude of the frequency response function of these two filters, the frequency axis being truncated between 0 and 20 Hz for clarity.

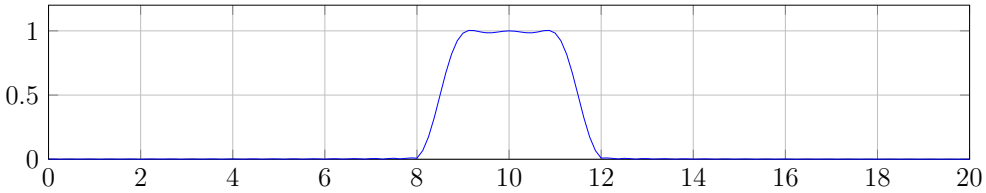

(a) bandpass filter

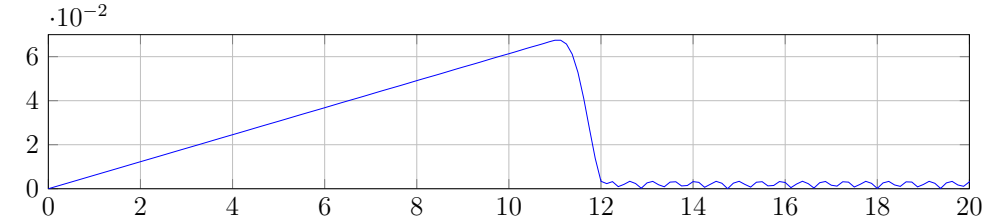

(b) differentiator filter

Figure 4: Frequency response function of the two filters for $f_0 = 10$ Hz.

The results obtained by the proposed algorithm applied to the previous synthetic signal are shown in Fig. 5. The noisy signal $\mathbf{x}$ is represented in Fig. 5a and the corresponding trajectory in Fig. 5g, where the influence of noise is clearly visible. The bandpass filtered signal $\mathbf{r}$ is shown in Fig. 5b and the corresponding trajectory in Fig. 5h, where the noise has been significantly reduced by the frequency-selective filter. The continuous change in amplitude and phase is visible in these two figures, where its influence on the shape of the trajectory and therefore on its geometric properties is particularly highlighted. Figures 5c to 5f show the estimated geometric properties where black curves correspond to theoretical values. As expected, $\|\mathbf{r}(t)\|$ and $\kappa(t)$ are time-varying because of the elliptical shape of the trajectory. The variations of these two geometric properties are greater before the change

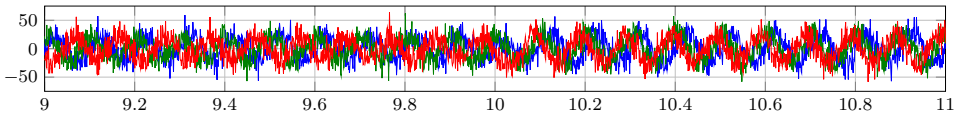

(a) $\mathbf{x}(t)$

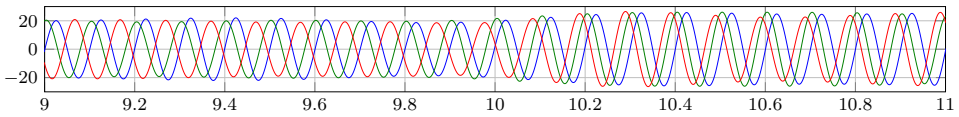

(b) $\mathbf{r}(t)$

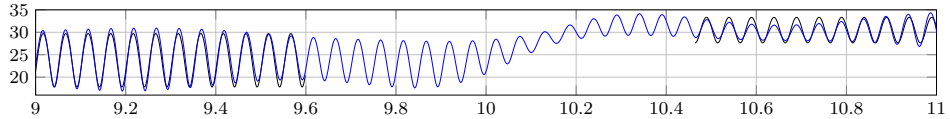

(c) $\widehat{\|\mathbf{r}(t)\|}$

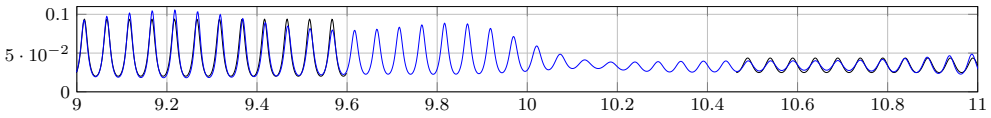

(d) $\widehat{\kappa(t)}$

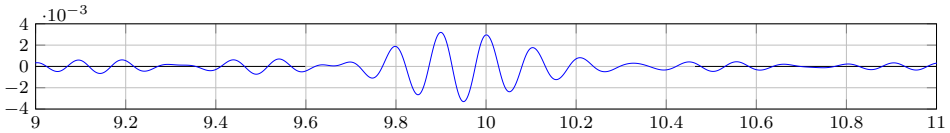

(e) $\widehat{\tau(t)}$

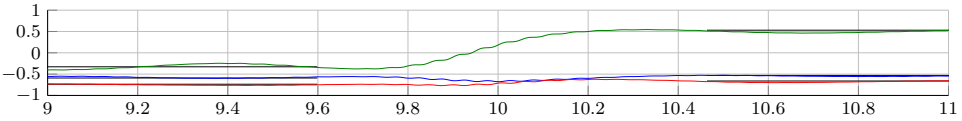

(f) $\widehat{\mathbf{B}(t)}$ in Cartesian coordinates

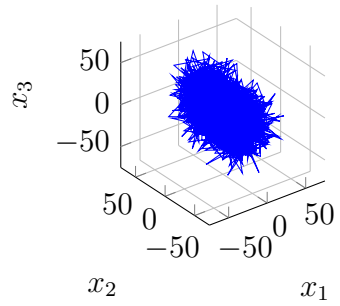

(g) $\mathbf{x}(t)$ in the 3D Euclidian space

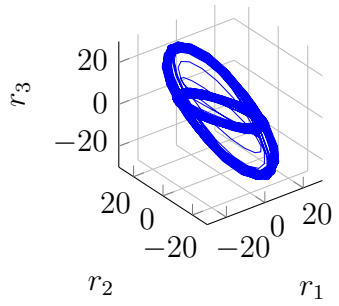

(h) $\mathbf{r}(t)$ in the 3D Euclidian space

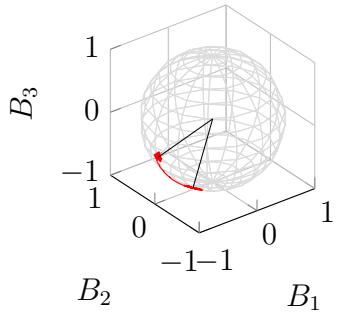

(i) $\widehat{\mathbf{B}(t)}$ in the 3D Euclidian space

Figure 5: Simulated noisy three-component sinusoidal signal $\mathbf{x}(t)$ with its main geometric properties.

than after, showing that the ellipse of the trajectory followed by $\mathbf{r}$ is flatter before the change than after. Figures 5e and 5f show that τ and $\mathbf{B}$ are approximately constant when amplitudes and phases stay constant. The torsion and binormal vector being related to the osculating plane, this means that the trajectory has a constant osculating plane during these parts of the signal. However, $\mathbf{B}$ has different coordinates before and after the change, corresponding to two different osculating planes. The theoretical values of these two directions of $\mathbf{B}$ are visible in Fig. 5i and drawn as two black lines, while the estimated values of $\mathbf{B}$ are plotted in red. Finally, the torsion τ takes large values only during the change where the osculating plane moves, and could be useful as a simple and efficient change detector.

The performance of the proposed algorithm seems to be good for estimation and tracking the geometric properties of three-component sinusoidal signals, although small estimation errors exist. In order to quantify these errors and clarify their origin, the influence of different parameters on the estimation performance of this algorithm is detailed in the following section.

3.3. Estimation performance

The estimation performance of the proposed algorithm as well as its limits once applied to a three-component sinusoidal signal are discussed in this section. Three parameters influencing the accuracy of the method have been identified:

- the amount of noise present in the original three-component signal,
- the fundamental frequency of the three-component sinusoidal signal to analyze,
- the ellipticity of the corresponding three-dimensional trajectory.

Three separate tests are therefore carried out where in each test, two of the parameters remain fixed while the third one varies within a given range of values. The three-component sinusoidal signal used for these tests is a 40-second discrete-time signal $\mathbf{y}$ with a mathematical expression given in Eq. (14).

$$\mathbf{y} = \begin{bmatrix} A_1 \sin\left(2\pi f_0 k/f_s + \varphi_1\right) \\ A_2 \sin\left(2\pi f_0 k/f_s + \varphi_2\right) \\ A_3 \sin\left(2\pi f_0 k/f_s + \varphi_3\right) \end{bmatrix} \quad \text{where } k \in \mathbb{N} \tag{14}$$

Its sampling frequency f_s is 256 Hz and its fundamental frequency is $f_0 < 128$ Hz. All three sinusoids have the same amplitude $A_1 = A_2 = A_3 = 20$ to obtain the same amount of signal whatever the component. The phases $[\varphi_1, \varphi_2, \varphi_3]$ are set to obtain a given flatness of the ellipse, measured by the ratio b/a where b is its semiminor axis and a its semimajor axis. In that case, $b/a = 0$ corresponds to a line segment trajectory and $b/a = 1$ to a circular trajectory. A centered and stationary white Gaussian noise is then added to this pure sinusoidal signal with the same variance whatever the component, the amount of which being measured by the global signal-to-noise ratio SNR computed for one component and expressed in dB. The range of values of the different parameters for the three performance tests are summarized in Table 1.

	SNR (dB)	f_0 (Hz)	b/a
Test 1	0 – 50	10	0.5994
Test 2	20	1 – 127	0.5994
Test 3	20	10	0.0741 – 1

Table 1: Range of values of the three parameters for the performance tests.

Concerning filters, the frequency-selective filter is a bandpass filter with a central frequency equal to f_0, a bandwidth of 2 Hz and a transition band of 1 Hz. The bandwidth of the partial-band differentiator filter ends at $f_0 + 1$ Hz and its stopband starts at $f_0 + 2$ Hz, corresponding to a transition band of 1 Hz.

The estimation performance is measured using the mean squared errors (MSE) of $\widehat{\|\mathbf{r}\|}$, $\widehat{\mathbf{B}}$, $\widehat{\kappa}$ and $\widehat{\tau}$, the estimates of the four geometric properties of interest $\|\mathbf{r}\|$, $\mathbf{B}$, κ and τ. Moreover, in order to facilitate the comparison between the different cases, the normalized MSE (NMSE) is computed when possible. These quantities are defined in the following equations for discrete-time signals where N represents the total number of samples of the signals.

$$\mathrm{NMSE}_{\widehat{\|\mathbf{r}\|}} = \frac{\sum_{k=1}^{N} \left(\|\mathbf{r}\,[k]\| - \widehat{\|\mathbf{r}\,[k]\|} \right)^2}{\sum_{k=1}^{N} \|\mathbf{r}\,[k]\|^2} \tag{15}$$

$$\mathrm{NMSE}_{\widehat{\kappa}} = \frac{\sum_{k=1}^{N} \left(\kappa\,[k] - \widehat{\kappa\,[k]} \right)^2}{\sum_{k=1}^{N} \kappa\,[k]^2} \tag{16}$$

$$\mathrm{NMSE}_{\widehat{\mathbf{B}}} = \frac{\sum_{i=1}^{3} \left(\frac{1}{N} \sum_{k=1}^{N} \left(\mathbf{B}_i - \widehat{\mathbf{B}_i\,[k]} \right)^2 \right)}{\sum_{i=1}^{3} \mathbf{B}_i^2} = \sum_{i=1}^{3} \left(\frac{1}{N} \sum_{k=1}^{N} \left(\mathbf{B}_i - \widehat{\mathbf{B}_i\,[k]} \right)^2 \right) \tag{17}$$

$$\mathrm{MSE}_{\widehat{\tau}} = \frac{1}{N} \sum_{k=1}^{N} \widehat{\tau\,[k]}^2 \tag{18}$$

Equations (15) and (16) are used to compute the NMSE of the estimated norm and curvature of the three-component sinusoidal signal, respectively. Equation (17) takes into account the three components $\mathbf{B}_i$, $i \in [1, 2, 3]$ of the binormal vector to compute the global NMSE $\mathrm{NMSE}_{\widehat{\mathbf{B}}}$. For three-component sinusoidal signals, $\mathbf{B}$ is a constant unit vector as stated in the previous section, which explains why the $\mathbf{B}_i$'s are constant and $\sum_{i=1}^{3} \mathbf{B}_i^2 = 1$ in this equation. The MSE of the torsion estimator $\mathrm{MSE}_{\widehat{\tau}}$ is computed using Eq. (18), where the theoretical value of the torsion τ has been set to zero as expected for such signals. This also explains why this error is not normalized.

For each parameter value, averaged MSEs obtained after averaging over 1000 Monte Carlo simulations are computed and analyzed. The corresponding results are summarized

in Figure 6. Figure 6a shows these errors with respect to the SNR expressed in dB. As

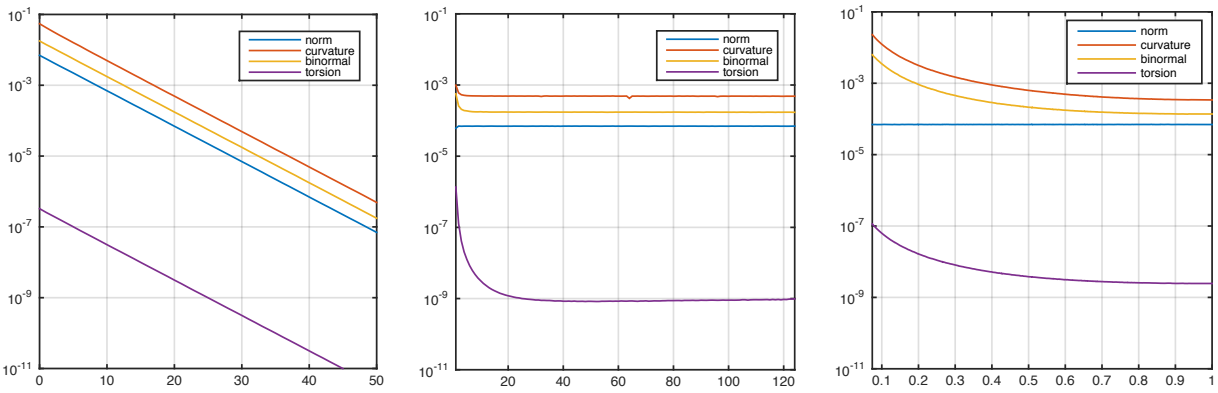

(a) test 1: errors versus SNR (b) test 2: errors versus f_0 (c) test 3: errors versus b/a

Figure 6: Averaged estimation errors $\mathrm{NMSE}_{\widehat{\|\mathbf{r}\|}}$, $\mathrm{NMSE}_{\widehat{\kappa}}$, $\mathrm{NMSE}_{\widehat{\mathbf{B}}}$ and $\mathrm{MSE}_{\widehat{\tau}}$ obtained for the three performance tests.

expected, the greater the SNR, the smaller the errors, and the linear shape shows that the different MSEs are all inversely proportional to the SNR in this range of values. It can be noticed that the worst estimation error is obtained for the curvature κ. This can be due to the fact that $\widehat{\kappa}$ is the only estimator that uses derivatives of $\mathbf{r}$ and estimates a time-varying quantity. Indeed, $\widehat{\|\mathbf{r}\|}$ estimates a time-varying quantity without differentiators, while $\widehat{\mathbf{B}}$ and $\widehat{\tau}$ need differentiators but estimate constant values. Figure 6b shows the same quantities with respect to the signal frequency f_0 expressed in Hertz. This figure shows that $\mathrm{NMSE}_{\widehat{\|\mathbf{r}\|}}$ is independent of f_0 while the other MSEs increase when f_0 is very small compared to the sampling frequency. Contrary to $\widehat{\|\mathbf{r}\|}$, estimators $\widehat{\mathbf{B}}$, $\widehat{\kappa}$, $\widehat{\tau}$ all use derivatives of $\mathbf{r}$, and this decrease in performance is mainly due to the FIR differentiator filters. Indeed, it has been shown in [12] that when the signal frequency f_0 is not much greater than the bandwidth of the bandpass filter, each differentiation step decreases the SNR because of the residual noise left by the bandpass filter, and finally deteriorates the global estimation performance of the algorithm. Figure 6c shows the influence of the ellipticity b/a on the estimation errors. Concerning $\mathrm{NMSE}_{\widehat{\kappa}}$, Eq. (7) shows that the denominator of the curvature $\kappa(t)$ is $\|\mathbf{r}'(t)\|^3$. Now, the flatter the ellipse, the faster $\|\mathbf{r}'(t)\|^3$ tends to zero at the tips of the ellipse, and as $\|\mathbf{r}'(t)\|$ tends to zero, $\kappa(t)$ becomes infinite and so does $\mathrm{NMSE}_{\widehat{\kappa}}$. In the worst-case scenario, the trajectory is a line segment, the flattest ellipse possible where $\|\mathbf{r}'(t)\| = 0$ at the tips where the curvature is impossible to estimate in this case. Concerning the estimation errors of the binormal vector $\mathrm{NMSE}_{\widehat{\mathbf{B}}}$ and of the torsion $\mathrm{MSE}_{\widehat{\tau}}$, they both increase the flatter the ellipse. When the ellipse is flatter, it tends to a line segment trajectory for which the osculating plane, the binormal vector and the torsion are not correctly defined. Therefore, it is not surprising that these quantities are difficult to estimate when the elliptical trajectory followed by the position vector flattens increasingly.

From these performance tests, several things should be kept in mind before applying this algorithm to experimental signals. A lot of noise in the measured signal deteriorates

the estimation performance of the algorithm, especially when the signal frequency is not greater than the bandwidth of the frequency-selective filter. Moreover, if the signal follows a trajectory that is almost a line or a very flat ellipse, this algorithm will produce higher estimation errors.

4. Bearing faults monitoring with three-axis vibration signals

In this section, the proposed algorithm is applied to vibration signals for bearing faults detection in rotating machines. The objective is to extract bearing fault indicators from the geometric characteristics of the trajectory followed by vibration signals measured in three orthogonal directions.

4.1. Experimental setup and datasets

The signals used in this section are measured on the test bench represented in Fig. 7. The

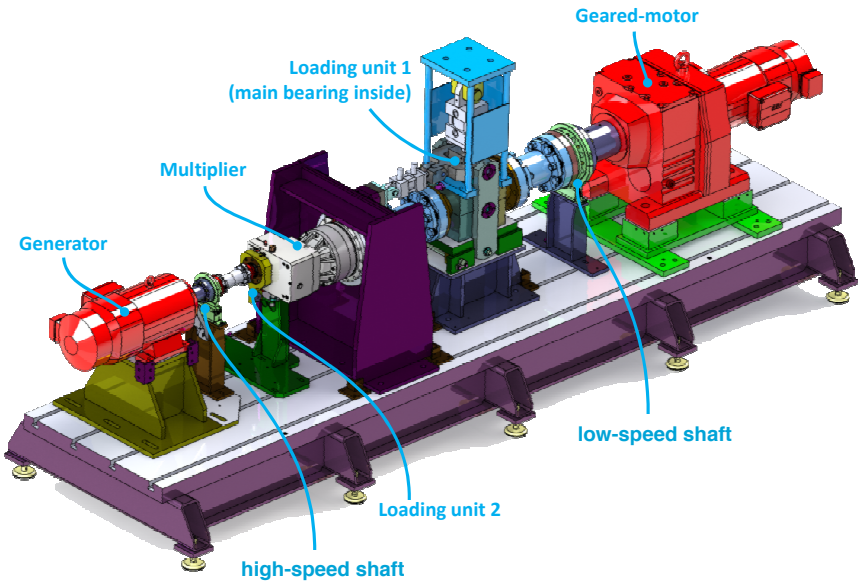

Figure 7: Structure of the test bench used for bearing faults monitoring [17].

kinematic chain consists in a low-speed shaft, a multiplier gearbox and a high-speed shaft. The output load is an induction generator and the operating conditions are determined by controlling the speed of the low-speed shaft thanks to a geared motor. This bench can be used to emulate the structure and behavior of a geared wind turbine, but also of an industrial system if the output generator is considered as a mechanical load. Loading unit 1 mounted on the low-speed shaft is used to accelerate the deterioration of the main bearing by applying radial and axial load to this component. The type of bearing used in the test is a radial spherical roller bearing with an inside diameter of 50 mm, on which natural faults may appear on any part, be it the inner race, outer race, bearing balls or cage.

Date	Event
October 7 2013	start of the 1st test
November 8 2013	fault appears
November 19 2013	end of the 1st test
December 16 2013	main bearing is replaced
December 17 2013	start of the 2nd test

Table 2: Main events and dates during the endurance tests of interest.

Several consecutive endurance tests were conducted with an alternation of degradation phases and measurement phases for which the rotational speed of the low-speed shaft was kept constant at 20 rpm. At the end of each test, the bearing was damaged up to an unknown degradation level and dismounted to visually characterize the level of damage. The period of time covered by this study starts on October 7 2013 and ends on January 31 2014. During this period, a natural fault appeared on November 8, the corresponding measurements were stopped on November 19, the faulty bearing was replaced with a new one on December 16 and a new measurement process started on December 17. Table 2 summarizes these events with the corresponding dates. Fig. 8 shows the state of the bearing at the end of the test used in this work, where localized spalling on the outer race is clearly visible.

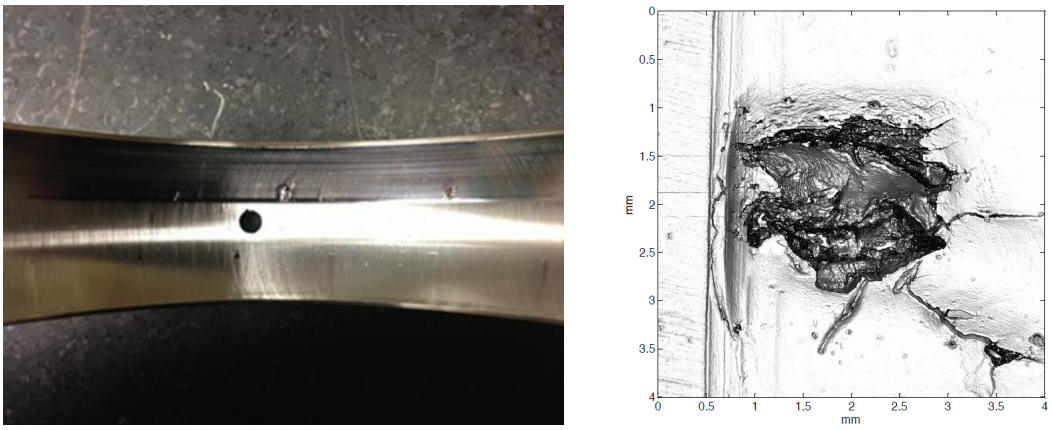

(a) outer race defects (b) detail of the largest defect

Figure 8: Spalling on the outer race of the bearing (courtesy of CETIM).

The data measured on this test bench and used in this work are vibration signals measured using three mono-axial accelerometers mounted on "loading unit 1" in three orthogonal directions in order to obtain the vibrations in the three directions of 3D Euclidean space. 20 datasets obtained between October 7 2013 and January 31 2014 are used. Each dataset consists in a three-component vibration signal of 1500 samples acquired with a sampling frequency of 100 Hz.

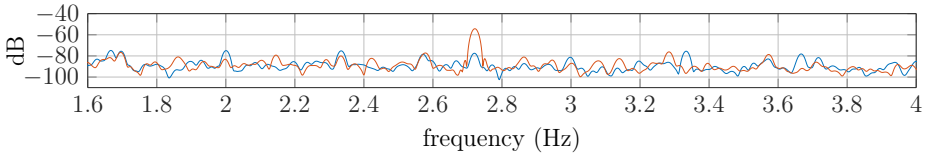

(a) 1st component

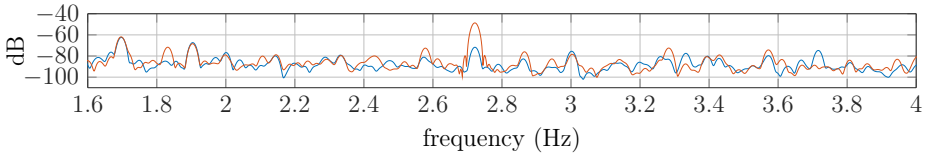

(b) 2d component

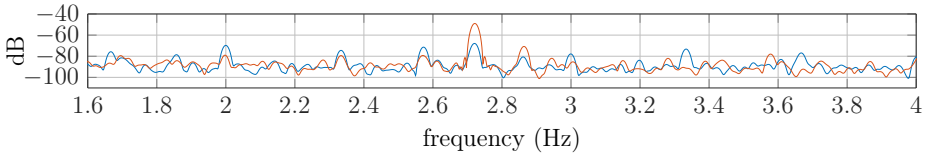

(c) 3rd component

Figure 9: Power spectral density of the three-axis vibration signal before (in blue) and after (in orange) the fault appeared.

4.2. Experimental results

First of all, the presence of the outer race fault during the test can be verified thanks to the power spectral density (PSD) of each component of the three-axis vibration signals before and after the fault appears. Indeed, bearings faults generate mechanical impacts and consequently vibrations with a frequency depending on the geometric characteristics of the bearing, the rotating speed of the shaft where the bearing is mounted on, and the type and location of the fault in the bearing. In this experiment, the expected outer race fault frequency of 2.72 Hz is clearly visible in Fig. 9 showing the PSD of each component for two datasets: in blue, the PSD of dataset November 7 2013 (before the fault appears), and in orange the PSD of dataset November 19 2013 (after the fault appears). This result confirms the presence of this particular fault in the monitored bearing before its visual inspection.

Next, the algorithm detailed in the previous section is applied to each dataset in order to estimate the time evolution of the four geometric properties of interest at different dates all along the test, and to analyze their behavior regarding the presence of the fault. Figures 10 and 11 show the results obtained for the two same datasets as previously: dataset November 7 2013 before the fault appears, and dataset November 19 2013 after the fault appears. These figures show vibration signals before and after frequency-selective filtering as well as the four geometric properties estimated by the algorithm. Figures 10a, 10g and 11a, 11g show that without the frequency-selective filter (a bandpass filter with a central frequency set to the fault frequency 2.72 Hz), no meaningful geometric information can be extracted from the data due to the presence of wide-band noise and several sinusoidal components. The signal

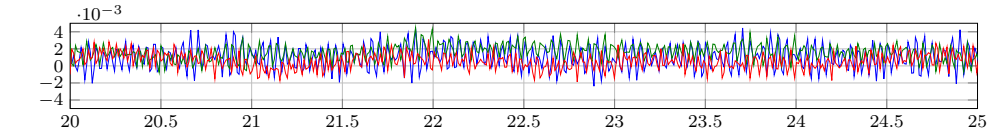

(a) $\mathbf{x}(t)$

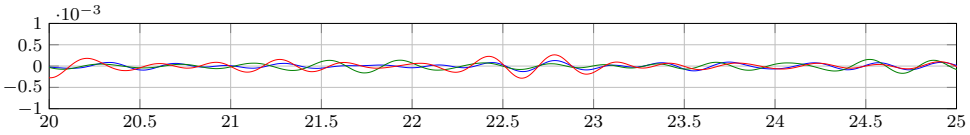

(b) $\mathbf{r}(t)$

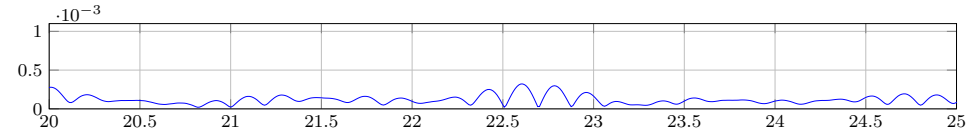

(c) $\widehat{\|\mathbf{r}(t)\|}$

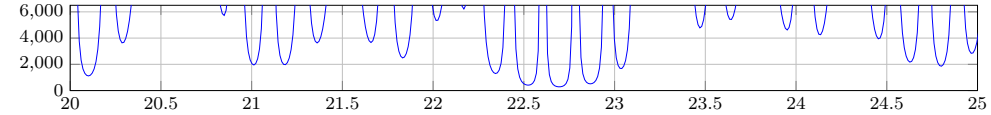

(d) $\widehat{\kappa(t)}$

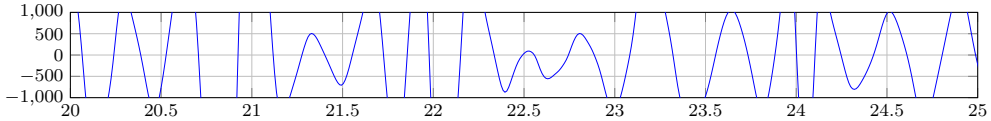

(e) $\widehat{\tau(t)}$

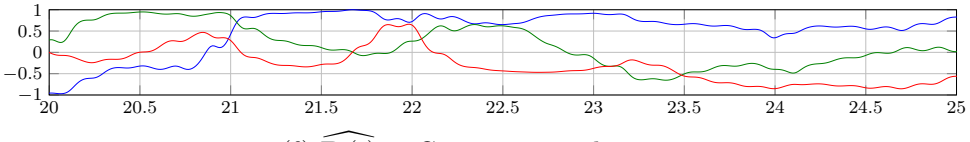

(f) $\widehat{\mathbf{B}(t)}$ in Cartesian coordinates

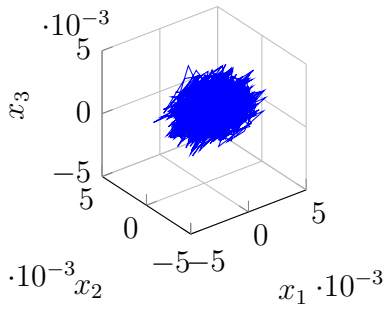

(g) $\mathbf{x}(t)$ in the 3D Euclidian space

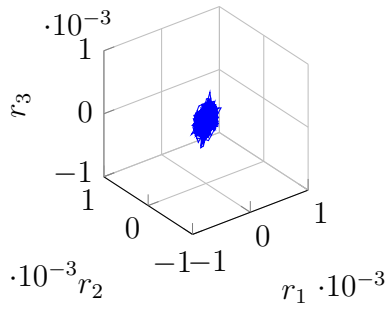

(h) $\mathbf{r}(t)$ in the 3D Euclidian space

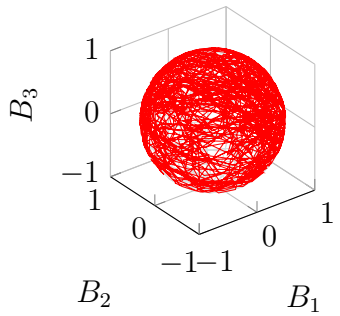

(i) $\widehat{\mathbf{B}(t)}$ in the 3D Euclidian space

Figure 10: Three-axis vibration signal before the bearing fault appears with its main geometric properties.

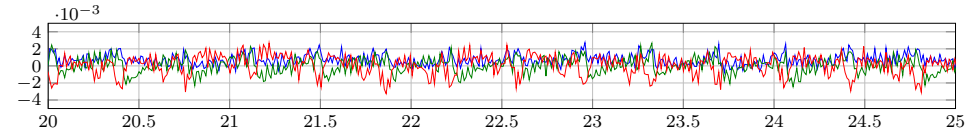

(a) $\mathbf{x}(t)$

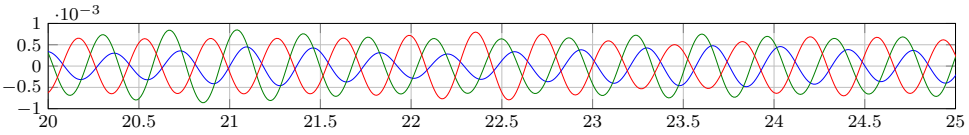

(b) $\mathbf{r}(t)$

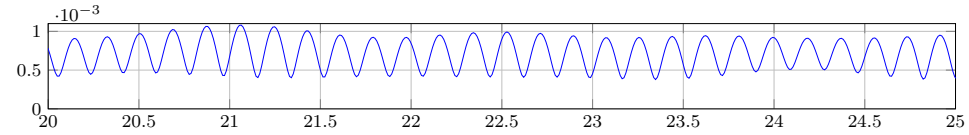

(c) $\widehat{\|\mathbf{r}(t)\|}$

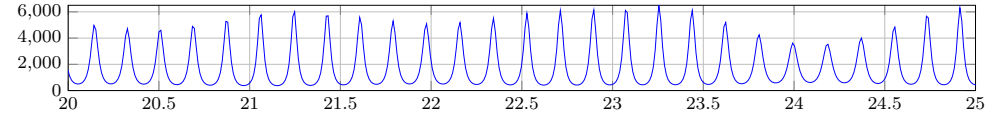

(d) $\widehat{\kappa(t)}$

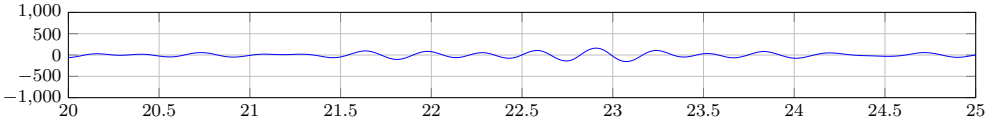

(e) $\widehat{\tau(t)}$

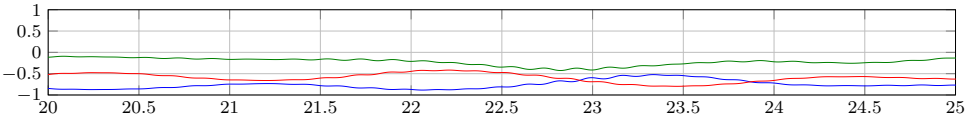

(f) $\widehat{\mathbf{B}(t)}$ in Cartesian coordinates

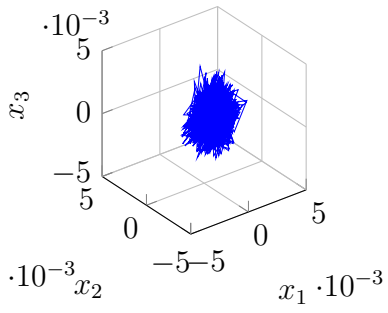

(g) $\mathbf{x}(t)$ in the 3D Euclidian space

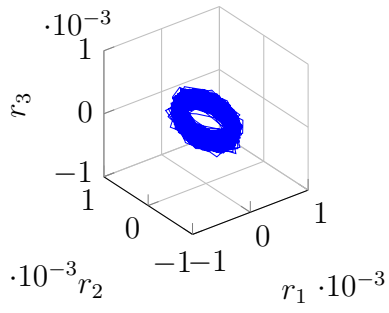

(h) $\mathbf{r}(t)$ in the 3D Euclidian space

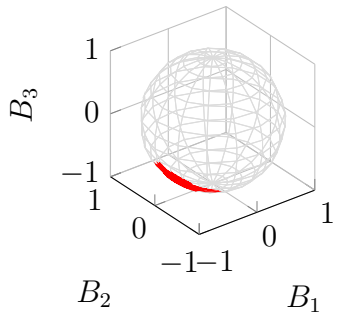

(i) $\widehat{\mathbf{B}(t)}$ in the 3D Euclidian space

Figure 11: Three-axis vibration signal after the bearing fault appears with its main geometric properties.

$\mathbf{r}(t)$ obtained after this necessary filtering step in shown in Fig. 10b, 10h and 11b, 11h. Before the fault appears, its 3D trajectory is completely unstructured in Fig. 10b and 10h, while a typical elliptical trajectory is clear in Fig. 11b and 11h once the fault appears. This remark is confirmed by the four geometric properties obtained for the two datasets. The signal norm in Fig. 10c and 11c show that $\|\mathbf{r}(t)\|$ increases in amplitude in case of a fault, because the amount of signal at the fault frequency increases as the fault appears. Notice also that $\|\mathbf{r}(t)\|$ has a more regular pattern after the fault appears, corresponding to a more structured 3D trajectory. The second geometric property, the curvature $\kappa(t)$ shown in Fig. 10d and 11d, behaves inversely. Before the fault appears, $\kappa(t)$ takes very large values and seems to fluctuate randomly, which represents a completely unstructured trajectory. When the fault appears, $\kappa(t)$ decreases and oscillates regularly around smaller values, which is expected since the 3D trajectory becomes more structured and elliptical in that case. The third geometric property, the torsion, is closely related to the variations of the binormal vector. As can be seen in Fig. 10e, the torsion $\tau(t)$ reflects the frequent and big changes in the binormal vector $\mathbf{B}(t)$, highlighting an unstructured shape for the trajectory. However, in Fig. 11e, $\tau(t)$ takes smaller values, corresponding to a more steady trajectory plane. The fourth and last geometric property is the binormal vector $\mathbf{B}(t)$ shown in Fig. 10f, 10i and 11f, 11i. From these figures, it can be seen that before the fault appears, $\mathbf{B}(t)$ does not point in a particular direction and varies randomly all along the measurement. Once the fault appears, it points in a stable direction, orthogonal to the plane that the 3D trajectory of $\mathbf{r}(t)$ is in. Finally, the results obtained before the fault appears and represented in Fig. 10 can be summarized as follows: $\|\mathbf{r}(t)\|$ shows that there is no significant signal at the fault frequency while $\kappa(t)$, $\tau(t)$ and $\mathbf{B}(t)$ show that the corresponding 3D trajectory has no structured shape. On the contrary, once the fault appears, the same quantities represented in Fig. 11 lead to the opposite conclusion: $\|\mathbf{r}(t)\|$ indicates that there is a significant component at the fault frequency and $\kappa(t)$, $\tau(t)$ and $\mathbf{B}(t)$ indicate that the resulting trajectory has a structured elliptical shape with almost constant characteristics.

Different bearing fault indicators can be proposed using the previous results, and several have been studied in [12]. One particularly interesting indicator quantifying the variations of the binormal vector is its standard deviation, defined has the square root of the sum of the variances of each of its components. As seen through the previous experimental results, this vector is nearly constant in the faulty case and varies strongly and randomly in the healthy case. Therefore, its standard deviation should be close to zero in the faulty case and should take large values in the healthy case. This is verified in Fig. 12 where this quantity has been computed for each dataset measured during the endurance test, and where the two vertical red lines mark when the bearing defect appears and when the faulty bearing is replaced by a new one. Another interesting property clearly visible in this figure is that this indicator is bounded between 0 and 1. This maximal value is due to the fact that the binormal vector is a unit vector with components bounded between ± 1. Indeed, before the fault appears, the corresponding 3D trajectory is unstructured and there is no preferred direction pointed to by the binormal vector as illustrated in Fig. 10f and 10i. In that case, the binormal vector can be thought of as a random variable with each of its components following a uniform probability distribution between ± 1. Their variance is therefore equal to $1/3$ and

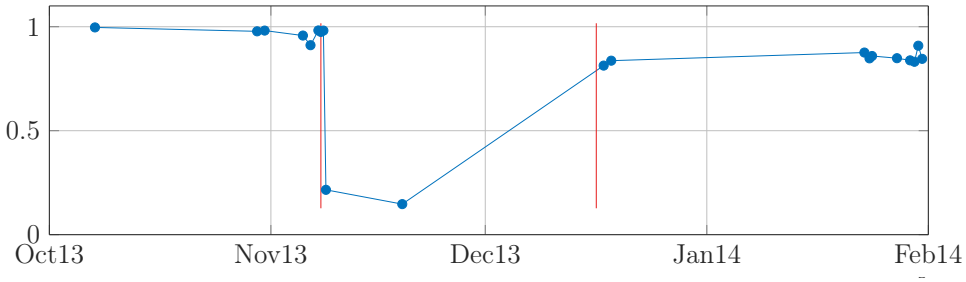

Figure 12: Standard deviation of the binormal vector obtained for each dataset during the endurance test (left red line: bearing defect appears, right red line: bearing replaced).

the standard deviation of $\mathbf{B}(t)$ previously defined is then equals to 1. On the contrary, when a fault occurs, the binormal vector is nearly constant and its standard deviation stays close to zero. These experimental results show that the type of information provided by the geometric properties of interest are different in nature and complementary. The signal norm $\|\mathbf{r}(t)\|$ is connected to the amount of signal at the fault frequency as well as to the shape of the trajectory. The curvature $\kappa(t)$ gives information about the shape of the trajectory, such as the flatness of the ellipse. The binormal vector $\mathbf{B}(t)$ gives the plane the trajectory is in, whereas the torsion $\tau(t)$ shows when this plane changes. These geometric informations can be used to deeply characterize the detected faults, but they can also be used to detect the presence of a fault in the monitored bearing as shown at the end of this section.

The next section presents a different experimental application of these tools.

5. Voltage dips monitoring with three-phase voltage signals

This section concerns the application of the proposed algorithm to the monitoring of voltage dips in three-phase power networks. These phenomena are the most common type of power-quality disturbances, and lead to important economic losses and distorted quality of industrial products [18]. Thus, voltage dips monitoring has become an essential requirement for power quality monitoring in power networks, and several methods have been developed to detect and characterize such disturbances [19, 20]. However, most of these techniques consider three-phase measurements as three separate one-dimensional quantities, and process each phase voltage independently from each other. In [7], a first step is taken where the three-phase quantities are considered two-dimensional after a Clarke transform [21], and are processed as complex-valued signals. In this section, the proposed method is applied in order to consider the three-phase voltages as a single three-dimensional quantity. The objective, if not to obtain better results than previously proposed methods, is to adopt a different and complementary point of view by considering three-phase voltages as a whole and gain additional information in the process.

The proposed algorithm is applied to an experimental three-phase voltage signal $\mathbf{x}(t)$ with a fundamental frequency $f_0 = 50$ Hz and sampled at $f_s = 3200$ Hz. This data, measured at one point of a high-voltage power network, is represented in Fig. 13a. It clearly undergoes a voltage dip between $t = 50$ ms and $t = 120$ ms with the dip being more pronounced for the

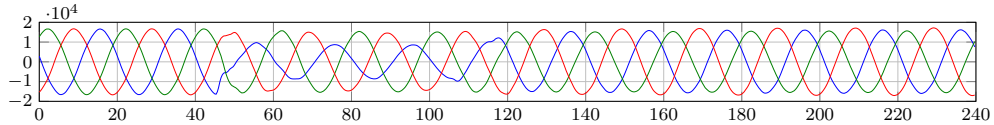

(a) $\mathbf{x}\,(t)$

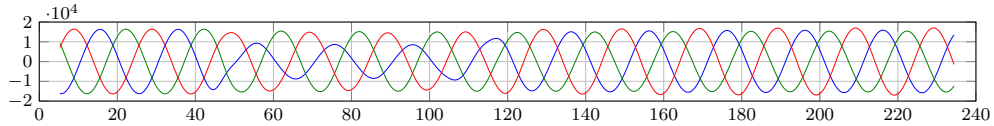

(b) $\mathbf{r}\,(t)$

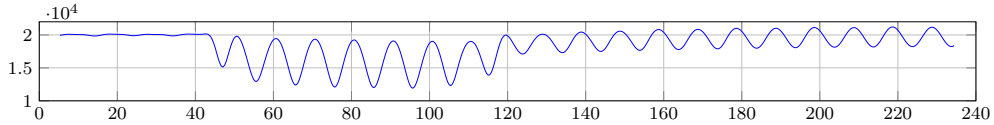

(c) $\widehat{\|\mathbf{r}\,(t)\|}$

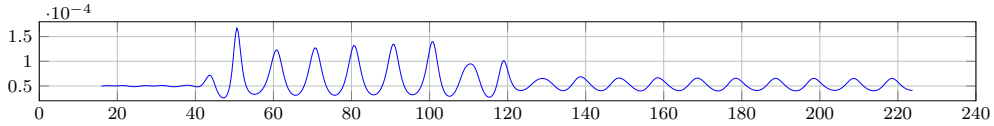

(d) $\widehat{\kappa\,(t)}$

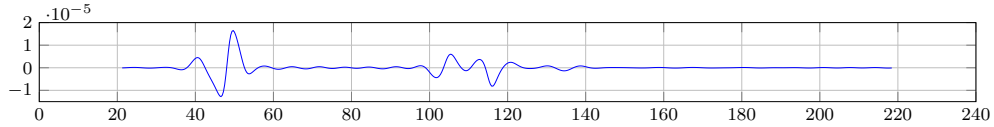

(e) $\widehat{\tau\,(t)}$

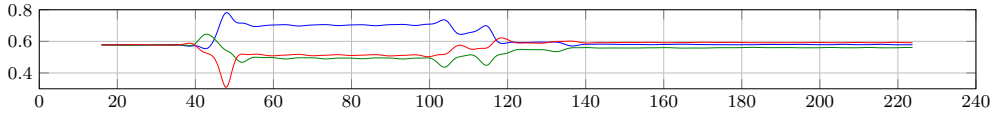

(f) $\widehat{\mathbf{B}\,(t)}$ in Cartesian coordinates

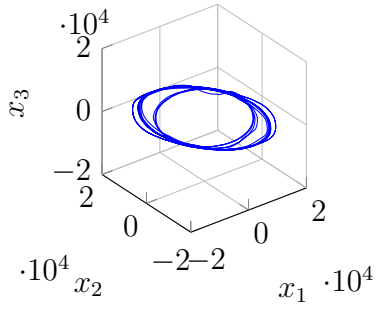

(g) $\mathbf{x}\,(t)$ in the 3D Euclidian space

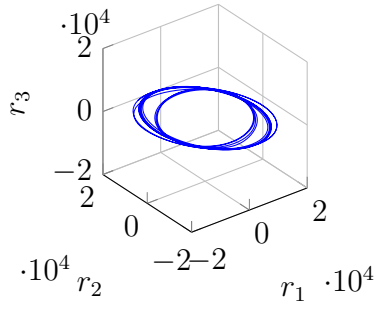

(h) $\mathbf{r}\,(t)$ in the 3D Euclidian space

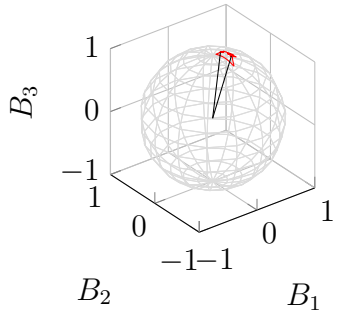

(i) $\widehat{\mathbf{B}\,(t)}$ in the 3D Euclidian space

Figure 13: Experimental three-phase voltage signal $\mathbf{x}\,(t)$ containing a voltage dip with its main geometric properties (time t in ms).

blue voltage. The corresponding three-dimensional trajectory is shown in Fig. 13g, where a change in the trajectory can also be seen. Voltage signals measured in power networks are very specific, and mostly consist in one large sine wave called the fundamental component, added to smaller harmonics, the closest and most significant being the 5^{th} and 7^{th} [18]. This particularity can be used to simplify the first step of the proposed algorithm. Instead of a bandpass filter, a simple lowpass filter is sufficient to separate the fundamental component from the others and obtain the desired three-component sinusoidal signal $\mathbf{r}(t)$. Since the fundamental frequency is 50 Hz, the passband of the lowpass filter is set to 60 Hz and its transition band to 200 Hz. Similarly, the passband of the differentiator filter ends at 60 Hz and its stopband starts at 260 Hz. The corresponding position vector $\mathbf{r}(t)$, shown in Fig. 13b, is then obtained at the output of the lowpass filter, and is represented as a moving point in 3D Euclidean space in Fig. 13h. These figures show that $\mathbf{r}(t)$ rotates around the origin with frequency $f_0 = 50$ Hz, and that the three-dimensional trajectory followed by $\mathbf{r}(t)$ changes during the measurement – clearly there are two different osculating planes – due to the voltage dip.

Next, the four geometric properties of $\mathbf{r}(t)$ are estimated using the proposed algorithm. The estimated signal norm, curvature, torsion and binormal vector are shown in Fig. 13c to 13f respectively. Notice that the torsion takes significant values only at the beginning and at the end of the voltage dip. Apart from these special periods of time, the torsion remains small and close to zero. Geometrically, this means that the 3D trajectory followed by $\mathbf{r}(t)$ stays in a fixed plane, except at these specific periods of time during which the osculating plane changes significantly. Notice also that the osculating plane containing the trajectory during and outside the voltage dip is not the same. This is confirmed by changes in the binormal vector: its Cartesian coordinates plotted in Fig 13f clearly take different values during and outside the voltage dip, which is confirmed by its 3D representation in Fig 13i. The curvature provides a different kind of information, related to the shape of the trajectory followed by $\mathbf{r}(t)$. Outside the voltage dip, the curvature is nearly constant so the trajectory is circular, which is what the trajectory of a balanced three-phase voltage should be. Indeed, a balanced three-phase voltage $\mathbf{v}$ can be written in the form of Eq. (19), corresponding to a circular trajectory of radius $\sqrt{\frac{3}{2}}V$ and thus of constant curvature.

$$\mathbf{v}(t) = \begin{bmatrix} V\cos(2\pi f_0 t + \varphi) \\ V\cos\left(2\pi f_0 t + \varphi - \frac{2\pi}{3}\right) \\ V\cos\left(2\pi f_0 t + \varphi - \frac{4\pi}{3}\right) \end{bmatrix} \tag{19}$$

During the dip, the curvature varies with frequency $2f_0 = 100$ Hz, i.e. twice per revolution. When the curvature in Fig. 13d is compared to the signal norm in Fig. 13c, it is clear that when $\mathbf{r}(t)$ is close to the origin, the curvature is small and vice versa. This corresponds to a trajectory with an elliptical shape. Therefore, the curvature shows that the trajectory of $\mathbf{r}(t)$ changes from a circle outside the dip to an ellipse during the dip.

The results obtained through this experimental data set show that geometric properties lead to important geometric information concerning the three-dimensional trajectory followed by $\mathbf{r}(t)$ and through this, provide information about the state of the corresponding

three-phase system. In other words, the proposed algorithm can be used to analyze the geometric changes in the trajectory of three-phase voltages as well as to detect and also possibly characterize voltage dips. More specifically, the torsion τ can be used for dip detection as it only takes significant values when there is a change in the osculating plane, indicating that there is a change in the system. The detected dips can then be characterized thanks to the osculating plane given by the coordinates of the binormal vector $\mathbf{B}$. Along with the signal norm $\|\mathbf{r}\|$ and the curvature κ, this leads to information about the shape of the trajectory during the dips.

6. Conclusions

With the objective of condition monitoring, this article proposes a method of estimating the geometric properties of the trajectory followed by a three-component sinusoidal signal in three-dimensional Euclidean space, along with a simple and efficient estimation algorithm. The proposed method is applied to two types of experimental data: three-axis vibration signals measured on a rotating machine and used for bearing fault monitoring, and voltage signals measured on a three-phase power network and used for voltage dips monitoring. The estimated geometric properties of the three-dimensional elliptical trajectory followed by these signals reflect the bearing faults and the voltage dips to be detected. From these results, it can be concluded that the proposed method is useful as it gives different and complementary information to existing condition monitoring methods.

Several improvements to the method can be considered in future works. The noise removal and frequency selection step can be further developed and improved so that the noise is removed more precisely and the frequency component is isolated more accurately. Certain geometric properties such as the semimajor axis, semiminor axis as well as the orientation in space of the obtained ellipse can be estimated in order to complete the geometric information given by the algorithm. In addition, the proposed method could be extended to more complex deterministic signals such as periodic signals containing more than a single sinusoidal component and even further, to random signals. It can also be noticed that the geometric approach relying on Frenet-Serret frame and formulas have been generalized to signals with any number of components [22, 23]. This allows to consider the application of the proposed method to signals with a number of components higher than three, even if in this case the geometric meaning of the obtained indicators is not so simple to analyze.

Concerning applications, the results already obtained for voltage dips and bearing faults detection could be taken a step further. More particularly, the estimated geometric properties could by used to classify the detected voltage dips or deeply characterize the detected bearing fault. Indeed, the geometric properties of vibration signals are directly connected to the three-dimensional movements of the rotating machine they are measured from, and thus have clear physical significations. For example the main direction of vibration, which is reflected thanks to the binormal vector defining the plane of the elliptical trajectory, can be used to deduce the direction in which the bearing is vibrating.

Acknowledgments

The authors would like to thank CETIM (Centre Technique des Industries Mécaniques) for providing the test-bench and experimental data.

References

[1] D. R. Brillinger, Time Series: Data Analysis and Theory, Society for Industrial and Applied Mathematics (SIAM), 2001.

[2] P. Granjon, Complex-valued signal processing for condition monitoring, in: Fifth International Conference on Condition Monitoring and Machinery Failure Prevention Technologies, Edinburgh, United Kingdom, 2008.

[3] P. J. Schreier, L. L. Scharf, Statistical Signal Processing of Complex-Valued Data: The Theory of Improper and Noncircular Signals, Cambridge University Press, 2010.

[4] N. Bachschmid, P. Pennacchi, A. Vania, Diagnostic significance of orbit shape analysis and its application to improve machine faults detection, Journal of the Brazilian Society of Mechanical Sciences and Engineering 26 (2) (2004) 200–208.

[5] C. W. Lee, Y. S. Han, The directional Wigner distribution and its applications, Journal of Sound and Vibration 216 (4) (1998) 585–600.

[6] Y. S. Han, C. W. Lee, Directional Wigner distribution for order analysis in rotating/reciprocating machine, Mechanical Systems and Signal Processing (MSSP) 13 (5) (1999) 723–737.

[7] V. Ignatova, P. Granjon, S. Bacha, Space vector method for voltage dips and swells analysis, IEEE Transactions on Power Delivery 24 (4) (2009) 2054–2061.

[8] M. P. do Carmo, Differential Geometry of Curves and Surfaces, Prentice Hall, 1976.

[9] B. O'Neill, Elementary Differential Geometry, Academic Press, 1966.

[10] E. Cartan, La théorie des groupes finis et continus et la géométrie différentielle, traitées par la méthode du repère mobile, Gauthier-Villars, 1937.

[11] M. Spivak, A Comprehensive Introduction to Differential Geometry, 2nd Edition, Vol. 2, Publish or Perish, 1979.

[12] G. S.-L. Phua, Estimation of geometric properties of three-component signals for condition monitoring, Theses, Université Grenoble Alpes (Jan. 2016).
URL https://tel.archives-ouvertes.fr/tel-01295193

[13] E. Wolf, Introduction to the Theory of Coherence and Polarization of Light, Cambridge University Press, 2007.

[14] G. Phua, P. Granjon, Estimation of geometric properties of three-component sinusoidal signals for system monitoring, in: The 7th International Conference on Acoustical and Vibration Methods Development and Applications for Surveillance and Diagnostics (Surveillance 7), 2013.

[15] J. G. Proakis, D. G. Manolakis, Digital Signal Processing: Principles, Algorithms, and Applications, 4th Edition, Pearson Education, 2007.

[16] C.-C. Tseng, S.-L. Lee, Linear phase FIR differentiator design based on maximum signal-to-noise ratio criterion, Signal Processing 86 (2) (2006) 388–398.

[17] N. Bédouin, S. Sieg-Zieba, Endurance testing on a wind turbine test bench: a focus on slow rotating bearing monitoring, in: Twelfth International Conference on Condition Monitoring and Machinery Failure Prevention Technologies, Oxford, United Kingdom, 2015.

[18] M. H. J. Bollen, Understanding Power Quality Problems: Voltage Sags and Interruptions, Wiley-IEEE Press, 2000.

[19] M. H. J. Bollen, I. Y. H. Gu, Signal Processing of Power Quality Disturbances, Wiley-IEEE Press, 2006.

[20] M. H. J. Bollen, L. D. Zhang, Different methods for classification of three-phase unbalanced voltage dips due to faults, Electric Power Systems Research 66 (1) (2003) 59–69.

[21] J. M. Aller, A. Bueno, T. Paga, Power system analysis using space-vector transformation, IEEE Transactions on Power Systems 17 (4) (2002) 957–965.
[22] C. Jordan, Sur la théorie des courbes dans l'espace à n dimensions, Comptes-rendus de l'Académie des sciences 79 (1874) 795–797.
[23] P. Griffiths, On cartan's method of lie groups and moving frames as applied to uniqueness and existence questions in differential geometry, Duke Mathematical Journal 4 (1974) 775–814.